

A Navier-Stokes-Peridynamics hybrid algorithm for the coupling of compressible flows and fracturing materials

Mingshuo Han^{a,b,1}, Shiwei Hu^{a,1}, Tianbai Xiao^{a,b,*}, Yonghao Zhang^{a,b,*}

^a*Centre for Interdisciplinary Research in Fluids, Institute of Mechanics, Chinese Academy of Sciences, Beijing, 100190, China*

^b*School of Engineering Science, University of Chinese Academy of Sciences, Beijing, 100049, China*

Abstract

Modeling and simulation of fluid-structure interactions are crucial to the success of aerospace engineering. This work addresses a novel hybrid algorithm that models the close coupling between compressible flows and deformable materials using a mesoscopic approach. Specifically, the high-speed flows are described by the gas-kinetic scheme, which is a robust Navier-Stokes alternative solver built on the molecular kinetic theory. The deformation, damage, and fracture of materials are depicted using the bond-based peridynamics, which serves as coarse-grained molecular dynamics to construct non-local extensions of classical continuum mechanics. The evolution of fluids and materials are closely coupled using the ghost-cell immersed boundary method. Within each time step, the solutions of flow and solid fields are updated simultaneously, and physics-driven boundary conditions are exchanged for each other via ghost cells. Extensive numerical experiments, including crack propagation in a pre-cracked plate, subsonic flow around the NACA0012 airfoil, supersonic flow around the circular cylinder, and shock wave impacting on the elastic panel, are performed to validate the algorithm. The simulation results demonstrate the unique advantages of current hybrid algorithm in solving fracture propagation induced by high-speed flows.

Keywords: Peridynamics; computational fluid dynamics; fluid-structure interaction; immersed boundary method; gas-kinetic scheme.

1. Introduction

The impact of multi-physics coupling on aerodynamic performance becomes increasingly significant on long-endurance and high-maneuverability aircraft [1]. Among others, fluid-structure interaction (FSI) is a typical example of multi-physics coupling problems [2]. As the speed and altitude of aircraft increase, the enhanced compressibility leads to intricate flow structures, which causes difficulties in calculation of the stress and heat flux acted on the structure. The irregular aerodynamic forcing and heating loads can cause deformation,

*Corresponding authors: txiao@imech.ac.cn, yonghao.zhang@imech.ac.cn

¹These authors contributed equally to this work.

Table 1: Nomenclature.

FSI	fluid-structure interaction
GKS	gas-kinetic scheme
BBPD	bond-based Peridynamics
t, \mathbf{x}	time and space variables
\mathbf{v}, ζ	particle velocity and internal energy variables
f	particle distribution function
Q	collision operator in the kinetic equation
g	Maxwellian equilibrium distribution function
τ	relaxation time
$\rho, \mathbf{V}, T, \lambda$	primitive flow variables
\mathbf{P}, \mathbf{q}	stress tensor and heat flux
ψ	collision invariants
\mathbf{W}	conservative flow variables
ρ_s	solid density
\mathbf{u}	displacement
δ	horizon radius
\mathbf{f}	force density vector
\mathbf{b}	body density vector
ξ, η	relative position and displacement vectors
ω	micropotential
s	bond stretch
c	micromodule function
$\bar{\mathbf{W}}$	cell-averaged conservative variables
\mathbf{F}^W	numerical fluxes for conservative variables
$\Delta \mathbf{S}$	area vector of cell faces
g_0, f_0	initial equilibrium and non-equilibrium distributions in GKS
a, b, A	normal, tangetial, and temporal derivatives in GKS
ν, β	volume and surface effect correction factors
GC	ghost cell
IP	imaginary point
BI	boundary intersection
\mathbf{n}_s	outward unit normal vector at boundary

damage, fracture and failure of the material of the vehicle, which in turn inversely affect the flow evolution. Such coupling effects often emerge in an extremely nonlinear manner under the flight condition. Accurate modeling and simulation of fluid-structure interactions are the key to the success of aerospace engineering [3].

To simulate FSI problems, a common strategy is to combine the numerical methods, e.g., the finite volume method (FVM) for computational fluid dynamics (CFD) and the finite element method (FEM) for computational solid mechanics, through effective message passing. Such coupling can be performed in two methods. The first idea is to generate two sets of body-fitted meshes that are capable of Lagrangian movement and deformation, so that the location change of fluid-structure interface can be tracked [4, 5]. The second approach is to model the boundary effects on a uniform Eulerian mesh, i.e., the immersed boundary method (IBM) [6–8]. It has been widely regarded for the ease of implementation and flexibility in handling complex boundaries. Related studies have been carried out on rigid-body [9–12] and flexible-body dynamics [13–16] coupled with incompressible [17–20] and compressible flows [21–26].

Despite the success of IBM-based research on FSI problems, studies on structural failure under external flows are still scarce. A main cause for this phenomenon is the limitation of traditional FEM in handling fracture problems. Based on the partial differential equations in the continuum mechanics, the FEM model suffers from ill-defined derivatives around spatial discontinuities, e.g., fractures or defects in the computational domain. Remedial techniques have been proposed to address this challenge, including remeshing technique that conform the mesh to discontinuities dynamically [27, 28] and the extended finite element method (XFEM) that capture the behavior of discontinuities within elements by enriching the solution space with additional functions [29, 30]. Although these methods extend the capability of FEM to describe discontinuities solution, they also lead to a number of problems in terms of computational overhead, degraded accuracy, and handling multiple discontinuities.

Peridynamics (PD) is a systematic theory proposed for fracture mechanics [31]. Based on the material point description, it models, point by point, the accumulative effects of its interactions with all surrounding points within a certain range. Therefore, the PD theory replaces the local interactions described by differential equations in classical continuum mechanics with non-local interactions described by integral equations, thus circumventing the challenges posed by spatial discontinuities and non-differentiable fields. When the relative displacement between two material points exceeds a critical threshold, their mutual interactions disappear, allowing spontaneous fracture modeling. This computational framework provides a solid basis for modeling fracture generation and propagation as well as multi-crack interactions and branching phenomena [32–36]. With two decades of development, the PD theory and related computational methods have become an important alternative to FEM in fracture mechanics [37–44].

Efforts have been initiated to simulate FSI problems using peridynamics. Gao et al. combined peridynamics for structural deformation and peridynamic differential operators (PDDO) for fluid motion to investigate the interaction between weakly compressible fluids and structures, and a collision model is built to model the fluid-structure interface as a reflective boundary [45]. Behzadinasab et al. developed a coupled method integrating iso-

geometric analysis (IGA) with PD to study the interaction between blast-induced airflow and structures [46, 47]. Zhang et al. proposed a strongly coupled method that combines the lattice Boltzmann method (LBM) and PD to solve the incompressible flow-induced structural deformation and fracture [48]. Federico et al. established a coupling approach integrating IBM with ordinary state-based PD to investigate three-dimensional incompressible flow-induced structural deformation and fracture [49]. Kim et al. introduced an immersed peridynamics method based on the direct-forcing IBM to study large deformation and failure of hyperelastic materials under incompressible fluid flow [50].

Current FSI studies based on peridynamics are mainly focused on incompressible and weakly compressible flows. As the flow velocity increases, the effects of compressibility become increasingly significant. The evolution of the wave system, including shock and rarefaction waves, makes the mechanism of FSI more complex. This work addresses this gap by developing a closely coupled computational framework. It combines the gas-kinetic scheme for compressible Navier-Stokes flows [51–53] and the bond-based peridynamics for fracturable materials. The evolution of fluid and structure is coupled using the ghost-cell immersed boundary method. The developed framework is capable of high-fidelity and real-time simulation of flow-induced structural deformation and fracture.

The rest of the paper is structured as follows. Section 2 briefly introduces the basic theory of fluids and solids. Section 3 presents the formulation of the solution algorithm and its detailed implementations. Section 4 includes numerical experiments to demonstrate the performance of the current method. The last section presents concluding remarks. The nomenclature is presented in Table 1.

2. Theory of Fluids and Solids

2.1. Gas kinetic theory

Gas kinetic theory provides an insightful perspective for understanding non-equilibrium fluid transport and designing numerical schemes that are compatible with entropy-increasing processes. The Boltzmann equation and its simplified models describe the evolution of a many-particle system statistically based on the single-particle distribution function. The Boltzmann-BGK model [54] takes the form

$$\partial_t f + \mathbf{v} \cdot \nabla_{\mathbf{x}} f = \mathcal{Q}(f) = \frac{g - f}{\tau}, \quad (1)$$

where $f(t, \mathbf{x}, \mathbf{v}, \zeta)$ is the particle distribution function with respect to time, space, velocity, and internal energy modes. The collision operator is denoted by \mathcal{Q} , where τ is the collision time and g is the Maxwellian that corresponds to thermodynamic equilibrium state, i.e.

$$g = \rho \left(\frac{\lambda}{\pi} \right)^{\frac{N+3}{2}} \exp \left[-\lambda \left((\mathbf{v} - \mathbf{V})^2 + \zeta^2 \right) \right], \quad (2)$$

where ρ is the density, \mathbf{V} is the macroscopic velocity, and $\lambda = m/2kT$, with m being the molecular mass, k the Boltzmann constant, and T the temperature. The degrees of freedom

of internal energy takes $(5 - 3\gamma)/(\gamma - 1) + 1$, where γ is the adiabatic index. The internal variable in the equilibrium is thus given by $\zeta^2 = \zeta_1^2 + \dots + \zeta_N^2$. Note that the BGK model provides the fixed Prandtl number $\text{Pr} = 1$. This deficiency can be ameliorated by correcting the equilibrium distribution in Eq.(1), e.g., the Shakhov [55] and ES-BGK models [56].

The conservative variables can be derived by taking the moments of the distribution function over the velocity space, i.e.,

$$\mathbf{W} = \begin{pmatrix} \rho \\ \rho \mathbf{V} \\ \rho E \end{pmatrix} = \int \psi f d\Xi, \quad (3)$$

where E denotes the total energy density, ψ is the vector of collision invariants,

$$\psi = \left(1, \mathbf{v}, \frac{1}{2}(\mathbf{v}^2 + \zeta^2)\right)^T, \quad (4)$$

and $d\Xi = d\mathbf{v}d\zeta$.

It is known that the Euler and Navier-Stokes equations can be derived as the limits of solutions of the Boltzmann equation. Considering the first-order Chapman-Enskog expansion of f , i.e.,

$$f = g + f_1 = g - \tau(\partial_t g + \mathbf{v} \cdot \nabla_{\mathbf{x}} g), \quad (5)$$

we can take conservative moments of the BGK equation, which yields

$$\int \psi(\partial_t g + \mathbf{v} \cdot \nabla_{\mathbf{x}} g) d\Xi = \tau \int \psi(\partial_t f_1 + \mathbf{v} \cdot \nabla_{\mathbf{x}} f_1) d\Xi, \quad (6)$$

from which the Navier-Stokes equations can be obtained, i.e.,

$$\begin{aligned} \frac{\partial \rho}{\partial t} + \nabla_{\mathbf{x}} \cdot (\rho \mathbf{V}) &= 0, \\ \frac{\partial \rho \mathbf{V}}{\partial t} + \nabla_{\mathbf{x}} \cdot (\rho \mathbf{V} \otimes \mathbf{V}) - \nabla_{\mathbf{x}} \cdot \mathbf{P} &= 0, \\ \frac{\partial \rho E}{\partial t} + \nabla_{\mathbf{x}} \cdot (\rho E \mathbf{V}) - \nabla_{\mathbf{x}} \cdot (\mathbf{P} \cdot \mathbf{V}) + \nabla_{\mathbf{x}} \cdot \mathbf{q} &= 0, \end{aligned} \quad (7)$$

where \otimes denotes dyadic product. The stress tensor and heat flux are defined as

$$\mathbf{P} = \int_{\mathbb{R}^3} (\mathbf{v} - \mathbf{V}) \otimes (\mathbf{v} - \mathbf{V}) f d\mathbf{v}, \quad \mathbf{q} = \int_{\mathbb{R}^3} \frac{1}{2} (\mathbf{v} - \mathbf{V}) (\mathbf{v} - \mathbf{V})^2 f d\mathbf{v}. \quad (8)$$

Inserting Eq.(5) into the above equation gives the Newton's stress formula and Fourier's law, which naturally recovers the Navier-Stokes equations.

In the context of viscosity-dominated flows, the collision time τ is linked to the dynamic viscosity μ through the relation $\tau = \frac{\mu}{p}$. Conversely, for heat-conduction-dominated flows, the collision time is selected as $\tau = \frac{\kappa}{c_p p}$ to recover the heat conduction coefficient κ .

The Chapman-Enskog expansion provides a comprehensive and consistent description of equilibrium (inviscid Euler) and non-equilibrium (viscous) effects in the Navier-Stokes equations. No artificial assumptions other than the truncation order are made. A family of gas-kinetic schemes (GKS) [57–59] have been developed based on the evolutionary Chapman-Enskog solution within the framework of BGK equation. In this work, the GKS solver is employed to solve the evolution of compressible flows, see section 3.1 for details.

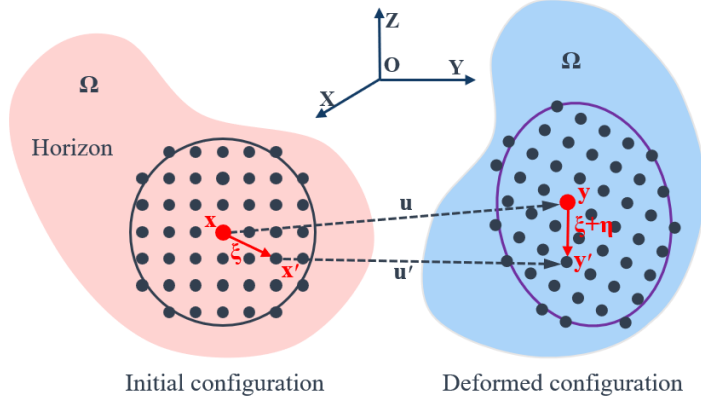


Figure 1: Illustration of BBPD and pairwise interaction between PD points. The horizon of the particle at the position \mathbf{x} encompasses all the PD particles interacting with it, and remains unchanged throughout deformation.

2.2. Peridynamic theory

Peridynamics is explicitly formulated based on Newton's second law of motion. The governing equation of bond-based Peridynamic (BBPD) can be written as

$$\rho_s(\mathbf{x})\ddot{\mathbf{u}}(t, \mathbf{x}) = \int_{H_{\mathbf{x}}} \mathbf{f}(\mathbf{u}' - \mathbf{u}, \mathbf{x}' - \mathbf{x})dV' + \mathbf{b}(t, \mathbf{x}), \quad (9)$$

where $\rho_s(\mathbf{x})$ denotes the mass density of solid at the position \mathbf{x} . The displacement is denoted as \mathbf{u} , and thus $\ddot{\mathbf{u}}$ is the acceleration vector field. The force density vector between the particles \mathbf{f} is a function of the relative position $\mathbf{x}' - \mathbf{x}$ and the relative displacement $\mathbf{u}' - \mathbf{u}$. The body force density vector is denoted as \mathbf{b} . The interactions between particles are modeled through integrals over the domain of influence. The integral domain (also known as horizon) is defined,

$$H_{\mathbf{x}} = \{\mathbf{x}' \in \mathbb{R} : |\mathbf{x} - \mathbf{x}'| < \delta\}, \quad (10)$$

where δ is the radius of horizon. The volume occupied by the particle at \mathbf{x}' is denoted as V' . After the configuration deformation, we denote the new positions of the particles as \mathbf{y}' and \mathbf{y} , where $\mathbf{y}' = \mathbf{x}' + \mathbf{u}'$ and $\mathbf{y} = \mathbf{x} + \mathbf{u}$. As shown in Figure 1, we introduce ξ and η to represent the relative position and displacement vectors between the particles \mathbf{x} and \mathbf{x}' , where $\xi = \mathbf{x}' - \mathbf{x}$ and $\eta = \mathbf{u}' - \mathbf{u}$.

For a microelastic material[31], a pairwise potential ω can be modeled such that

$$\mathbf{f}(\eta, \xi) = \frac{\partial \omega(\eta, \xi)}{\partial \eta}, \quad \forall \xi, \eta. \quad (11)$$

Under simple linear microelasticity, the micropotential is defined as

$$\omega(\eta, \xi) = \frac{cs^2 \|\xi\|}{2}, \quad (12)$$

where c represents the micromodule function, and s represents the bond stretch, i.e.,

$$s = \frac{\|\xi + \eta\| - \|\xi\|}{\|\xi\|}. \quad (13)$$

Therefore, the corresponding pairwise force \mathbf{f} becomes

$$\mathbf{f}(\eta, \xi) = \frac{\partial \omega(\eta, \xi)}{\partial \eta} = cs \|\xi\| \frac{\partial s}{\partial \eta} = cs \frac{\xi + \eta}{\|\xi + \eta\|}. \quad (14)$$

Here, the micromodule function c takes usually the constant form as

$$c = \begin{cases} \frac{2E}{\pi \delta^2 A}, & \text{for 1D,} \\ \frac{9E}{\pi \delta^3 h}, & \text{for plane stress,} \\ \frac{48E}{5\pi \delta^3 h}, & \text{for plane strain,} \\ \frac{12E}{\pi \delta^4}, & \text{for 3D.} \end{cases} \quad (15)$$

Failure of functional materials can be naturally formulated in the BBPD since it allows a bond to break when its stretch exceeds a predefined threshold. The tensile force in the bond is no longer sustained after the failure. Therefore, we modify the bond force density as

$$\mathbf{f} = \lambda_s cs \frac{\xi + \eta}{\|\xi + \eta\|}. \quad (16)$$

Here, λ_s is a history-dependent scalar valued function that describes the state of bond failure. When the bond stretch s exceeds the critical bond stretch s_c , the bond state are set to zero, i.e.,

$$\lambda_s = \begin{cases} 1.0, & \text{if } s < s_c, \\ 0.0, & \text{if } s \geq s_c. \end{cases} \quad (17)$$

The critical bond stretch s_c can be determined by the material's critical energy release rate G_c [60], i.e.,

$$s_c = \begin{cases} \sqrt{\frac{\pi G_c}{3k\delta}} & \text{for 2D,} \\ \sqrt{\frac{5G_c}{9k\delta}} & \text{for 3D,} \end{cases} \quad (18)$$

where k is the bulk modulus of the material.

3. Solution Algorithm

3.1. Gas-kinetic scheme

The gas-kinetic scheme is a finite volume method. The computational domain Ω is divided into N_x non-overlapping elements, and the cell-averaged conservative variables are introduced as

$$\bar{\mathbf{W}}_i = \frac{1}{V_i} \int_{\Omega_i} \mathbf{W}(t, \mathbf{x}) d\mathbf{x}. \quad (19)$$

Integrating Eq.(7) yields the update algorithm of $\bar{\mathbf{W}}$, i.e.,

$$\frac{\partial \bar{\mathbf{W}}_i}{\partial t} = -\frac{1}{V_i} \oint_{\partial \Omega_i} \mathbf{F}^W \cdot d\mathbf{S} = -\frac{1}{V_i} \sum_{k=1}^{N_f} \mathbf{F}_k^W \cdot \Delta \mathbf{S}_k, \quad (20)$$

where \mathbf{F}^W denotes the numerical fluxes, $\mathbf{S} = \mathbf{n}\Delta S$ is the area vector pointing out of the cell, and N_f is the number of faces.

The core task in the finite volume method is to accurately compute the numerical fluxes. For brevity, we employ the two-dimensional Cartesian coordinate system to introduce the principle of gas-kinetic flux solver. It can be straightforwardly extended to non-orthogonal mesh using local coordinate transformation.

Under the assumption that the collision time is a local constant, the integral solution of the BGK equation in Eq.(1) at a cell face $(x_{i+1/2}, y_j)$ writes

$$f(x_{i+1/2}, y_j, t, u, v, \zeta) = \frac{1}{\tau} \int_0^t g(x', y', t', u, v, \zeta) e^{-(t-t')/\tau} dt' + e^{-t/\tau} f_0(x_{i+1/2} - ut, y_j - vt), \quad (21)$$

where $x' = x_{i+1/2} - u(t - t')$, $y' = y_j - v(t - t')$ are the particle trajectories, f_0 is the initial distribution function at the beginning of each time step ($t = 0$). Two unknowns g and f_0 are constructed to concretize the above equation and construct the numerical fluxes. We assume, without loss of generality, that $x_{i+1/2} = 0$ and $y_j = 0$ to simplify the notation.

The initial distribution function is constructed following the piecewise Chapman-Enskog expansion, i.e.,

$$f_0 = \begin{cases} g^l (1 + a^l x + b^l y - \tau(a^l u + b^l v + A^l)), & x \leq 0 \\ g^r (1 + a^r x + b^r y - \tau(a^r u + b^r v + A^r)), & x > 0 \end{cases} \quad (22)$$

where g^l and g^r are the Maxwellian distributions related to the left and right-hand states around a face, while $\{a^l, a^r\}$ and $\{b^l, b^r\}$ are related to the slopes in the normal and tangential directions.

The equilibrium state is constructed as

$$g = g_0(1 + (1 - H(x))\bar{a}^l x + H(x)\bar{a}^r x + \bar{b}y + \bar{A}t), \quad (23)$$

where g_0 is the initial Maxwellian distribution at the face, while $\{\bar{a}^l, \bar{a}^r\}$ and \bar{b} are connected with the normal and tangential slopes of g . The $H(x)$ is the heaviside step function,

$$H(x) = \begin{cases} 0, & \text{if } x < 0, \\ 1, & \text{if } x \geq 0. \end{cases} \quad (24)$$

In both f and g , the slopes are related to the gradients of macroscopic variables via

$$\int f a \psi d\Xi = \partial_x \mathbf{W}, \quad \int f b \psi d\Xi = \partial_y \mathbf{W}, \quad (25)$$

and can then be determined by solving a linear system. Substituting Eqs.(22) and (23) yields the time dependent solution at the face,

$$\begin{aligned}
f(x_{i+\frac{1}{2}}, y_j, t, u, v, \xi) &= (1 - e^{-t/\tau})g_0 \\
&+ [\tau(-1 + e^{-t/\tau}) + te^{-t/\tau}] [\bar{a}^l H(u) + \bar{a}^r(1 - H(u))] u g_0 \\
&+ \tau \left(\frac{t}{\tau} - 1 + e^{-t/\tau} \right) \bar{A} g_0 \\
&+ e^{-t/\tau} [(1 - u(t + \tau)\bar{a}^l)H(u)g^l + (1 - u(t + \tau)\bar{a}^r)(1 - H(u))g^r] \\
&+ e^{-t/\tau} [-\tau A^l H(u)g^l - \tau A^r(1 - H(u))g^r].
\end{aligned} \tag{26}$$

The numerical fluxes can thus be computed by

$$\begin{pmatrix} F_\rho \\ F_{\rho U} \\ F_{\rho V} \\ F_{\rho E} \end{pmatrix}_{i+\frac{1}{2},j} = \int u \begin{pmatrix} 1 \\ u \\ v \\ \frac{1}{2}(u^2 + v^2 + \zeta^2) \end{pmatrix} f(x_{i+\frac{1}{2}}, j, t, u, v, \zeta) d\Xi. \tag{27}$$

3.2. Peridynamic solver

In the peridynamic solver, the solid region is discretized into a group of material points. The integral operator in Eq.(9) is approximated by the numerical quadrature. The semi-discrete governing equation of the bond-based peridynamics (BBPD) writes

$$\rho_s(\mathbf{x}_i)\ddot{\mathbf{u}}(t, \mathbf{x}_i) = \sum_{j=1}^{N_i} [\mathbf{f}_{i,j}(\mathbf{u}_j - \mathbf{u}_i, \mathbf{x}_j - \mathbf{x}_i)\beta_{i,j}\nu_{i,j}V_j] + \mathbf{b}(t, \mathbf{x}_i), \tag{28}$$

where N_i is the number of particles within the horizon of the particle located at \mathbf{x}_i . The subscript j denotes an arbitrary particle positioned at \mathbf{x}_j within the horizon of the particle at \mathbf{x}_i , and V_j is the volume of the particle at \mathbf{x}_j within the horizon of the particle at \mathbf{x}_i . For the simplest uniform distribution of points, $V_j = (\Delta x)^3$. Here, $\nu_{i,j}$ and $\beta_{i,j}$ are the correction factors for the volume and surface effects respectively for the particle at \mathbf{x}_j within the horizon of the particle at \mathbf{x}_i and Δx represents the particle spacing.

Based on Eq.(16), the spatially discrete form of the force density vector of each bond $\mathbf{f}_{i,j}$ satisfies

$$\begin{aligned}
\mathbf{f}_{i,j}(\mathbf{u}_j - \mathbf{u}_i, \mathbf{x}_j - \mathbf{x}_i) &= c_s \lambda_s \frac{\xi_{ij} + \eta_{ij}}{|\xi_{ij} + \eta_{ij}|} \\
&= c_s \lambda_s \frac{|\xi_{ij} + \eta_{ij}| - |\xi_{ij}|}{|\xi_{ij}|} \frac{\xi_{ij} + \eta_{ij}}{|\xi_{ij} + \eta_{ij}|} \\
&= c_s \lambda_s \frac{|\mathbf{y}_j - \mathbf{y}_i| - |\mathbf{x}_j - \mathbf{x}_i|}{|\mathbf{x}_j - \mathbf{x}_i|} \frac{\mathbf{y}_j - \mathbf{y}_i}{|\mathbf{y}_j - \mathbf{y}_i|}.
\end{aligned} \tag{29}$$

The explicit forward and backward difference scheme is employed as the integrator along the time direction. The dynamic evolution of displacement, velocity, and acceleration is

computed as

$$\begin{aligned}
\ddot{\mathbf{u}}_i^{(n)} &= \frac{\mathbf{f}_{i,j}^{(n)} + \mathbf{b}^{(n)}(\mathbf{x}_i, n\Delta t)}{\rho(\mathbf{x}_i)}, \\
\dot{\mathbf{u}}_i^{(n+1)} &= \dot{\mathbf{u}}_i^{(n)} + \ddot{\mathbf{u}}_i^{(n)} \Delta t, \\
\mathbf{u}_i^{(n+1)} &= \mathbf{u}_i^{(n)} + \dot{\mathbf{u}}_i^{(n+1)} \Delta t.
\end{aligned} \tag{30}$$

3.3. Immersed boundary method

The ghost-cell immersed boundary method (GCIBM) is employed to couple the evolution of the structure and the flow fluid. The schematic of the GCIBM method is shown in Figure 2. The boundary of the solid is represented by discrete body markers (depicted by purple pentagons) connected by linear segments, which distinguishes the fluid cells (depicted by green circles) and the solid cells (depicted by blue squares). The ghost cells (depicted by orange diamonds) are virtual points within the solid domain near the fluid-structure interface, facilitating the application of boundary conditions. Imaginary point (IP) nodes (depicted by black triangles) are symmetrically located across the boundary relative to the GC nodes, while boundary intersection (BI) nodes (depicted by magenta plus signs) are defined as the midpoints between the GC and their corresponding IP nodes.

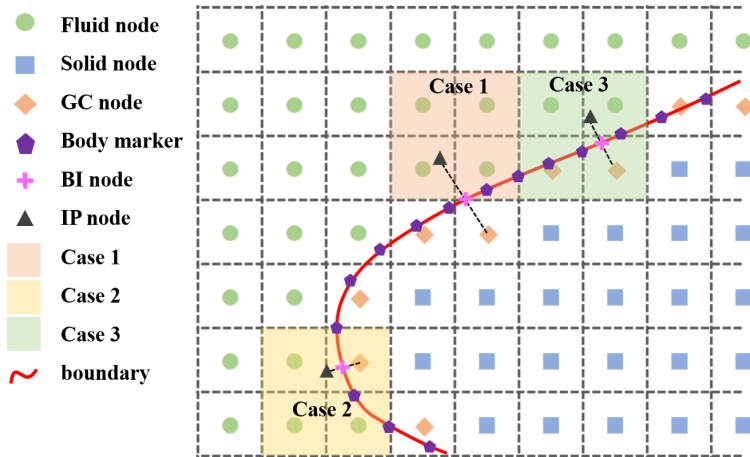


Figure 2: Schematic showing the GC-related nodes on the 2D fluid-structure boundary.

The key to GCIBM lies in calculating the pseudo flow variables in the GCs, which play a dual role in the simulation. On one hand, they are integral to flow simulation by enforcing the no-slip and no-penetration boundary conditions. On the other hand, variables defined at GCs, e.g., pressure, are used to compute the forces exerted on the solid boundary, which in turn serve as boundary conditions for PD, which is crucial for capturing fluid-structure interactions.

3.3.1. Identification of imaginary points and boundary intersections

After the determination of fluid and solid cells according to a given geometric shape, the location of IP and nodes can be determined via

$$\mathbf{x}_{\text{IP}} = \mathbf{x}_{\text{GC}} + 2d\mathbf{n}_s, \quad \mathbf{x}_{\text{BI}} = \frac{\mathbf{x}_{\text{IP}} + \mathbf{x}_{\text{GC}}}{2}, \quad (31)$$

where \mathbf{x}_{GC} , \mathbf{x}_{IP} , and \mathbf{x}_{BI} are the positions of the GC, IP, and BI nodes, respectively. Here, d is the shortest distance from the ghost cell to the boundary, and \mathbf{n}_s is the outward unit normal vector at the boundary.

3.3.2. Calculation of variables at boundary intersections

The BI nodes are typically positioned between boundary nodes (with possible overlap). The variables at the BI nodes can be computed using the Lagrange interpolation,

$$\phi_{\text{BI}} = \frac{(x_{\text{BI}} - x_2)(y_{\text{BI}} - y_2)}{(x_1 - x_2)(y_1 - y_2)}\phi_1 + \frac{(x_1 - x_{\text{BI}})(y_1 - y_{\text{BI}})}{(x_1 - x_2)(y_1 - y_2)}\phi_2, \quad (32)$$

where (x_1, y_1) and (x_2, y_2) denote the two neighboring boundary nodes.

3.3.3. Calculation of variables at imaginary points

The bi-linear interpolation method is used to compute any flow variable ϕ (e.g., pressure, velocity, and temperature) at the IP node. Such interpolation technique utilizes the information from the nearest neighboring fluid cells around the IP. The variables ϕ at the IP are expressed as

$$\phi = w_1 + w_2x_{\text{IP}} + w_3y_{\text{IP}} + w_4x_{\text{IP}}y_{\text{IP}}, \quad (33)$$

where w_i ($i = 1, 2, 3, 4$) are the interpolation coefficients, determined by the following Eq.(34) to (38) based on the indices of the neighboring fluid nodes.

If all four neighboring nodes are fluid nodes (Case 1 in Figure 2), the coefficients w_i are determined by:

$$\begin{bmatrix} w_1 \\ w_2 \\ w_3 \\ w_4 \end{bmatrix} = \begin{bmatrix} 1 & x_1 & y_1 & x_1y_1 \\ 1 & x_2 & y_2 & x_2y_2 \\ 1 & x_3 & y_3 & x_3y_3 \\ 1 & x_4 & y_4 & x_4y_4 \end{bmatrix}^{-1} \begin{bmatrix} \phi_1 \\ \phi_2 \\ \phi_3 \\ \phi_4 \end{bmatrix}, \quad (34)$$

where $\{x_i, y_i\}_{i=1,2,3,4}$ represents the locations of four neighboring fluid nodes around the IP, respectively.

If one of the four nodes belongs to the solid domain (Case 2 in Figure 2), the BI node replaces the solid node in the interpolation. Given the Dirichlet fluid-solid boundary condition, the coefficients w_i are calculated as

$$\begin{bmatrix} w_1 \\ w_2 \\ w_3 \\ w_4 \end{bmatrix} = \begin{bmatrix} 1 & x_1 & y_1 & x_1y_1 \\ 1 & x_2 & y_2 & x_2y_2 \\ 1 & x_3 & y_3 & x_3y_3 \\ 1 & x_{\text{BI}} & y_{\text{BI}} & x_{\text{BI}}y_{\text{BI}} \end{bmatrix}^{-1} \begin{bmatrix} \phi_1 \\ \phi_2 \\ \phi_3 \\ \phi_{\text{BI}} \end{bmatrix}, \quad (35)$$

where $(x_{\text{BI}}, y_{\text{BI}})$ and ϕ_{BI} represent the coordinates and interpolated values at the BI point, respectively. Given the Neumann-type boundary condition, where the flux is specified as $\hat{\mathbf{n}} \cdot \nabla \phi = h$, the bi-linear interpolation weights w_i ($i = 1, 2, 3, 4$) are computed by:

$$\begin{bmatrix} w_1 \\ w_2 \\ w_3 \\ w_4 \end{bmatrix} = \begin{bmatrix} 1 & x_1 & y_1 & x_1 y_1 \\ 1 & x_2 & y_2 & x_2 y_2 \\ 1 & x_3 & y_3 & x_3 y_3 \\ 0 & n_{x,\text{BI}} & n_{y,\text{BI}} & x_{\text{BI}} n_{y,\text{BI}} + y_{\text{BI}} n_{x,\text{BI}} \end{bmatrix}^{-1} \begin{bmatrix} \phi_1 \\ \phi_2 \\ \phi_3 \\ h \end{bmatrix}, \quad (36)$$

where $\hat{\mathbf{n}} = (n_{x,\text{BI}}, n_{y,\text{BI}})$ is the unit normal vector at the BI node, and $n_{x,\text{BI}}$ and $n_{y,\text{BI}}$ are its components along the x and y directions.

If two of the four nodes belong to the solid domain (Case 3 in Figure 2), the boundary intersection points (BI1 and BI2) replace the two solid nodes. Under the Dirichlet boundary condition, the interpolation coefficients w_i are determined by

$$\begin{bmatrix} w_1 \\ w_2 \\ w_3 \\ w_4 \end{bmatrix} = \begin{bmatrix} 1 & x_1 & y_1 & x_1 y_1 \\ 1 & x_2 & y_2 & x_2 y_2 \\ 1 & x_{\text{BI1}} & y_{\text{BI1}} & x_{\text{BI1}} y_{\text{BI1}} \\ 1 & x_{\text{BI2}} & y_{\text{BI2}} & x_{\text{BI2}} y_{\text{BI2}} \end{bmatrix}^{-1} \begin{bmatrix} \phi_1 \\ \phi_2 \\ \phi_{\text{BI1}} \\ \phi_{\text{BI2}} \end{bmatrix}, \quad (37)$$

where $(x_{\text{BI1}}, y_{\text{BI1}})$, $(x_{\text{BI2}}, y_{\text{BI2}})$, ϕ_{BI1} , and ϕ_{BI2} represent the coordinates and interpolated variables at the two BI points. For the Neumann-type boundary condition, where the fluxes at BI1 and BI2 are specified as g_1 and g_2 , respectively, the interpolation coefficients are computed by

$$\begin{bmatrix} w_1 \\ w_2 \\ w_3 \\ w_4 \end{bmatrix} = \begin{bmatrix} 1 & x_1 & y_1 & x_1 y_1 \\ 1 & x_2 & y_2 & x_2 y_2 \\ 0 & n_{x1,\text{BI1}} & n_{y1,\text{BI1}} & x_{\text{BI1}} n_{y,\text{BI1}} + y_{\text{BI1}} n_{x1,\text{BI1}} \\ 0 & n_{x2,\text{BI2}} & n_{y2,\text{BI2}} & x_{\text{BI2}} n_{y,\text{BI2}} + y_{\text{BI2}} n_{x2,\text{BI2}} \end{bmatrix}^{-1} \begin{bmatrix} \phi_1 \\ \phi_2 \\ g_1 \\ g_2 \end{bmatrix}. \quad (38)$$

The obtained interpolation weights w_i are then used to compute the variables at the IP nodes using Eq.(33).

3.3.4. Calculation of variables in ghost cells

Once the variables at the IP and BI nodes are determined corresponding to the given boundary conditions, the variables in the ghost cells can be calculated. For an arbitrary variable ϕ , governed by the Dirichlet boundary condition, the variables at GC nodes are calculated as

$$\phi_{\text{GC}} = 2\phi_{\text{BI}} - \phi_{\text{IP}}. \quad (39)$$

For pressure p , which is governed by the Neumann boundary condition, the status in the GC is given by $p_{\text{GC}} = p_{\text{BI}}$. And thus, using the ideal gas law, the density at the GC nodes is computed as $\rho_{\text{GC}} = \frac{p_{\text{GC}}}{RT_{\text{GC}}}$, where R is the gas constant. The solution algorithm of fluid-structure coupling is summarized in Figure 3.

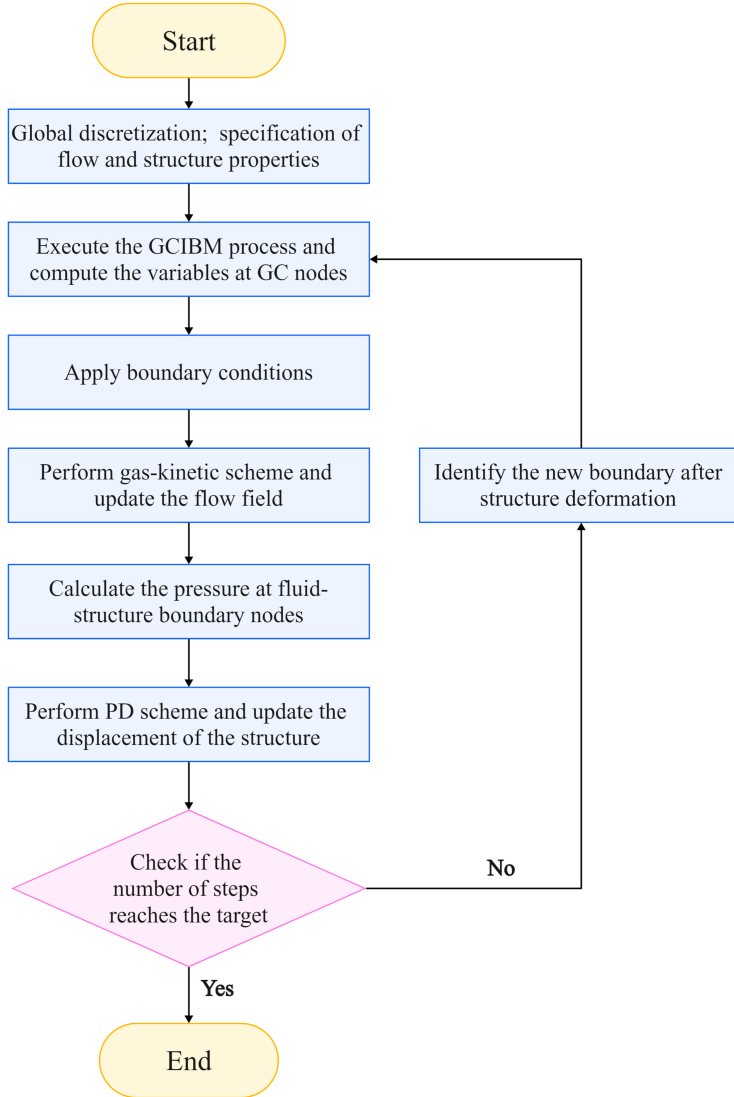


Figure 3: The solution algorithm of fluid-structure coupling.

4. Numerical Experiments

4.1. Validation of compressible flow solver

We first validate the gas-kinetic compressible flow solver along with the immersed boundary method. Two benchmark cases are employed as numerical experiments, i.e., the laminar flow around a NACA0012 airfoil and the supersonic flow around a circular cylinder.

4.1.1. Subsonic flow around a NACA0012 airfoil

The NACA0012 airfoil is considered at a zero angle of attack ($\alpha = 0^\circ$), with the freestream Mach number $Ma = 0.5$ and the Reynolds number $Re = 5000$. The computational domain spans $(-10D, 20D) \times (-10D, 10D)$, with the leading edge of the airfoil located at the origin.

A non-uniform Cartesian grid is employed. A fine grid ($\Delta x = \Delta y = D/512$) is used near the airfoil, while a coarser grid ($\Delta x = \Delta y = D/2$) is applied in more distant areas. Figure 4 shows the Mach number distribution around the airfoil. Figure 5 presents the comparison of the pressure coefficient distribution along the airfoil surface between the current results and those from the literature [61, 62]. The consistency between these results confirms the sufficiency of the current approach in accurately predicting viscous compressible flows with boundary effects.

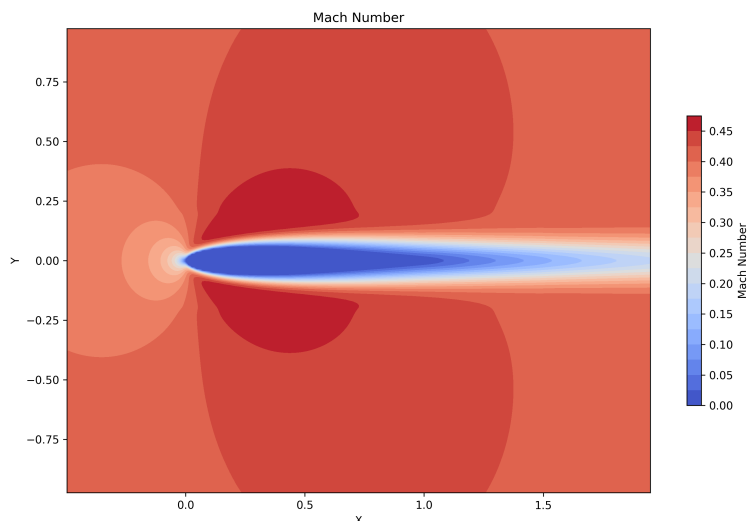


Figure 4: Mach number distribution in the flow field around the airfoil.

4.1.2. Supersonic flow around a circular cylinder

The supersonic flow around a circular cylinder is considered. The freestream Mach number is set as $Ma = 2.0$, and the Reynolds number, $Re = 300$. The computational domain spans $(0,10D) \times (0,12D)$, with the cylinder center located at $(2D,6D)$.

Similar as the airfoil case, a non-uniform grid is employed. A fine grid ($\Delta x = \Delta y = D/512$) is used near the cylinder surface, while a coarser grid ($\Delta x = \Delta y = D/2$) is applied in the distant regions. Figure 6 shows the Mach number distribution around the cylinder, and Figure 7 presents a comparison of the pressure coefficient distribution along the cylinder surface between the results from the current model and those from the literature [63]. The comparison of drag coefficients C_D from different numerical methods is shown in Table 2. The numerical experiments demonstrate that the current approach is capable of accurate prediction of the behavior of supersonic flow as it interacts with solid boundaries.

Table 2: Comparison of drag coefficient predicted by the current simulations with the reported data.

Method	Body-conformal[61]	IBM[63]	Current Simulation
C_D	1.547	1.525	1.556

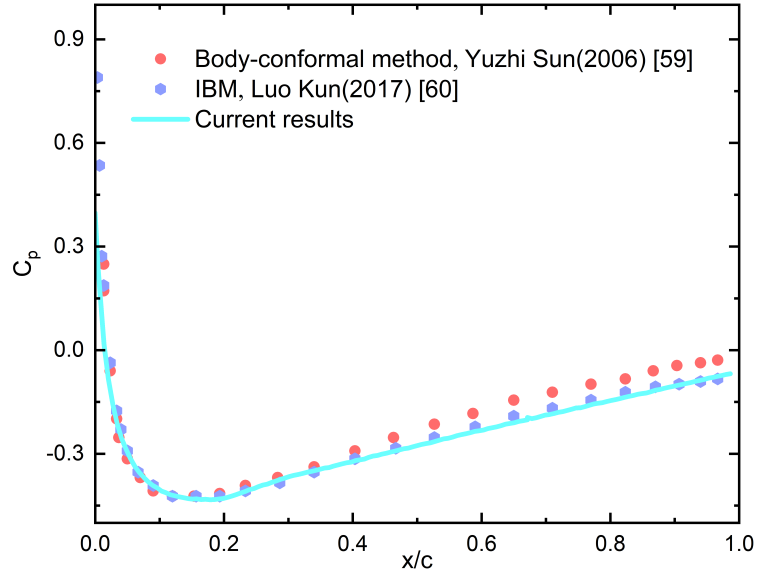


Figure 5: Comparison of the pressure coefficient distribution C_p along the airfoil surface, where the horizontal axis x/c represents the relative horizontal position along the airfoil, where c is the airfoil chord length, and the vertical axis C_p represents the pressure distribution.

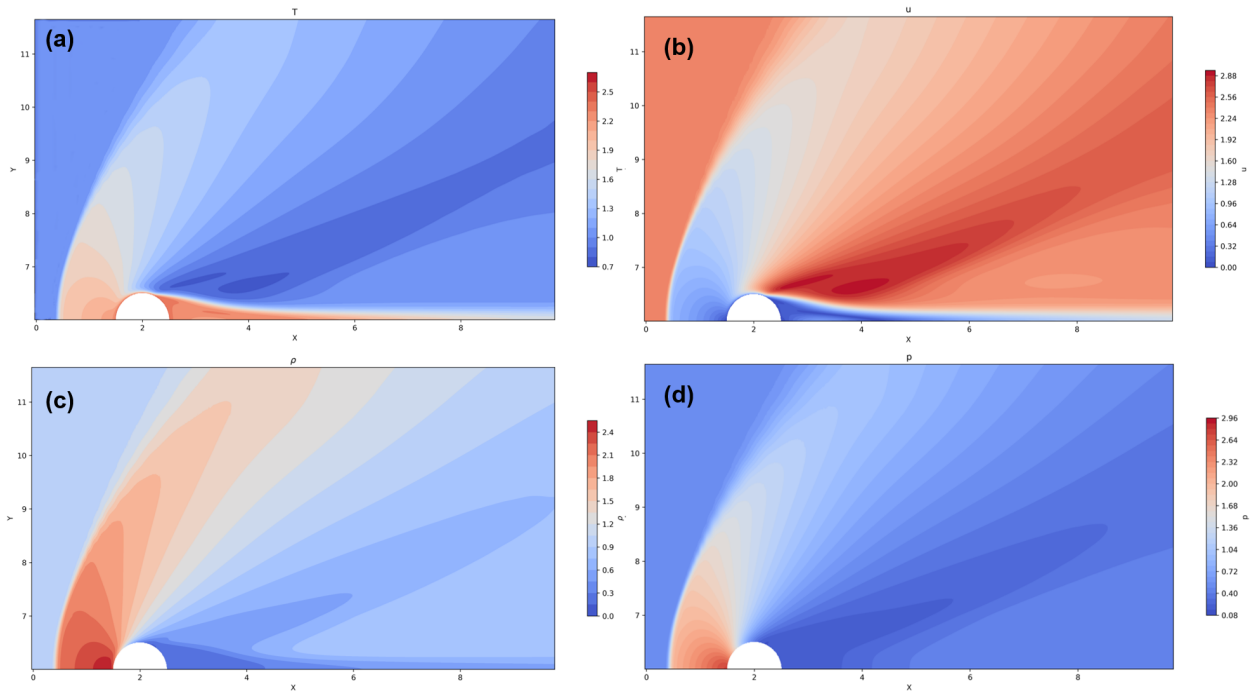


Figure 6: Distribution of solution fields in the supersonic flow around circular cylinder. (a) temperature; (b) velocity; (c) density; (d) pressure.

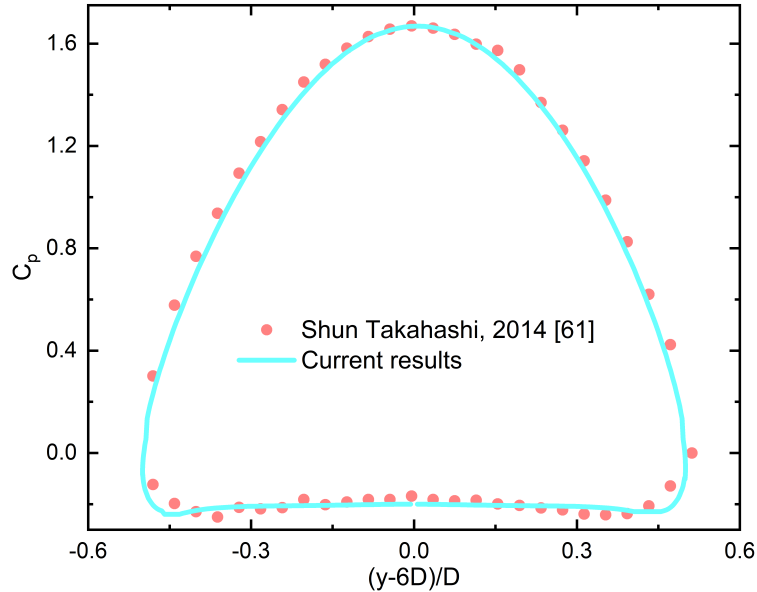


Figure 7: Comparison of the pressure coefficient distribution C_p along the cylinder surface between the results from the current model and those from the literature. In this figure, the horizontal axis $(y-6D)/D$ represents the relative vertical position along the cylinder, where D is the diameter of the cylinder, and the vertical axis C_p represents the pressure distribution.

4.2. Validation of peridynamic solver

We then validate the peridynamic model for structural deformation and crack propagation. A two-dimensional plate with an inherent crack is settled. The plate dimensions are $L = 50$ mm (length) and $W = 50$ mm (width). A horizontal crack of length $D = 10$ mm is initialized at the plate's center. The material is assumed to be isotropic and linear elastic with Young's modulus E of 192GPa and the density of 8000 kg/m^3 .

The plate is discretized into 500×500 material points. The velocity boundary conditions of $u_y = \pm 20$ m/s are applied along its upper and lower edges. Two fictitious boundary layers, R_c , each containing 500×3 material points, are added at the top and bottom to enforce the boundary condition. The simulation employs a time step of $\Delta t = 1.3367 \times 10^{-8}$ s. The schematic of the numerical experiment is shown in Figure 8.

The fracture behavior of the plate is governed by the critical stretch s_c . Figure 9 presents the comparison of the shape of cracks predicted by the current method and literature results at $s_c = 1.0$. Figure 10 provides the predicted fracture propagation velocity compared with the reference solution [48, 64]. The overall good agreement suggests that the current bond-based peridynamic solver can describe material deformation and damage.

4.3. Validation of the coupling scheme

Here, the fluid-structure interaction solver is to be validated using the experimental setup by Giordano [65]. The Giordano model features an elastic panel fixed at its lower edge to a rigid base. This setup is placed in a shock tube consisting of a movable high-

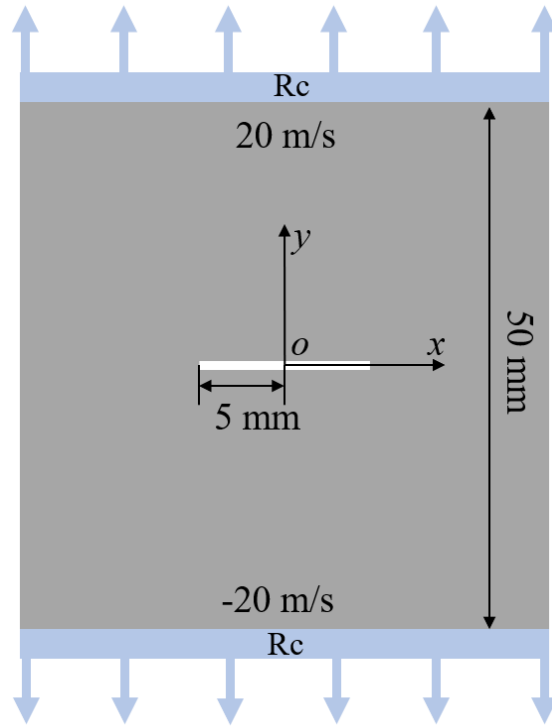


Figure 8: Schematic of the plate with a pre-existing crack.

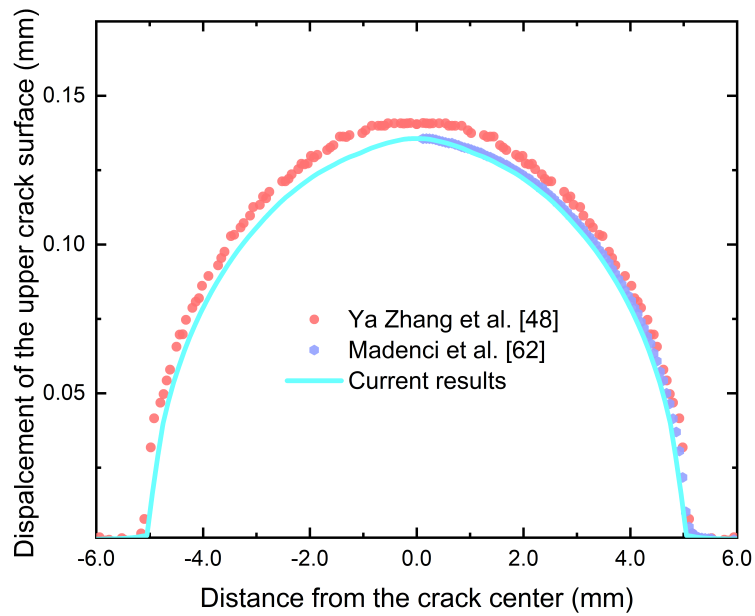


Figure 9: Vertical displacement of the material points near the upper surface of initial crack at the time $t = 16.7 \mu s$ when failure is not allowed.

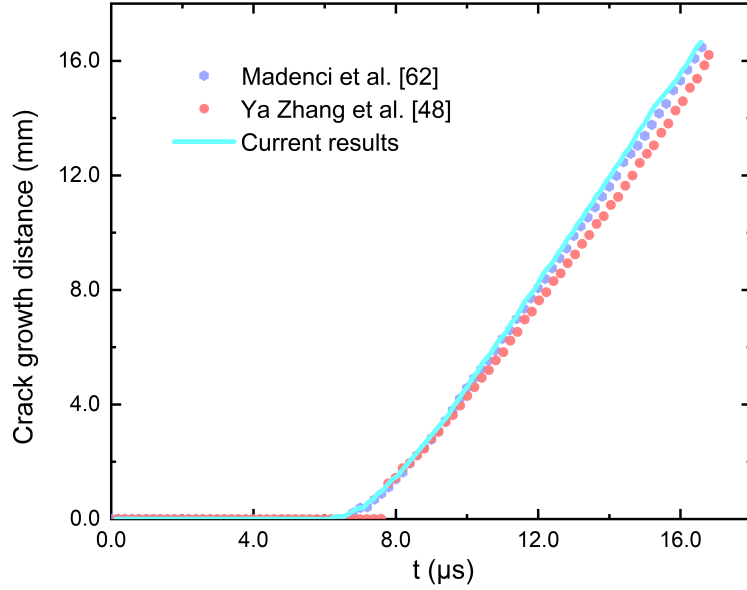


Figure 10: Variation in the propagation distance of the right crack tip during growth, when failure occurs.

pressure chamber (0.75 m long), a fixed low-pressure chamber (2.02 m long), and a movable experimental chamber (0.98 m long), as summarized in Figure 11.

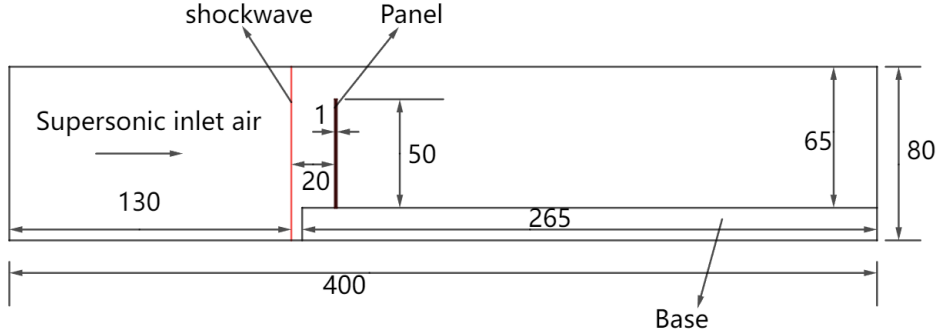


Figure 11: Schematic of the shock tube experiment.

Ning et al.[25] simplified the model by assuming a tube length of 300 mm with a positive shock imposed at the left boundary. The base was removed under the assumption that its impact on the results is negligible. In the simplified model, the panel has a length of 50 mm and a thickness of 1 mm, and its material behavior is linear elastic. The simplified experimental setup is illustrated in Figure 12. The initial flow field and material parameters are summarized in Table 3. The material of panel is assumed to be isotropic and linear elastic with Young's modulus E of 220 GPa and the density of 7850 kg/m^3 .

The computational domain spans $(0, 6L) \times (0, 1.3L)$. To reduce computational cost, a non-uniform grid is used in the x -direction, with finer grid spacing ($\Delta x = 0.002L$) near the plane and coarser grid spacing ($\Delta x = 0.02L$) farther away. Since the plane length is

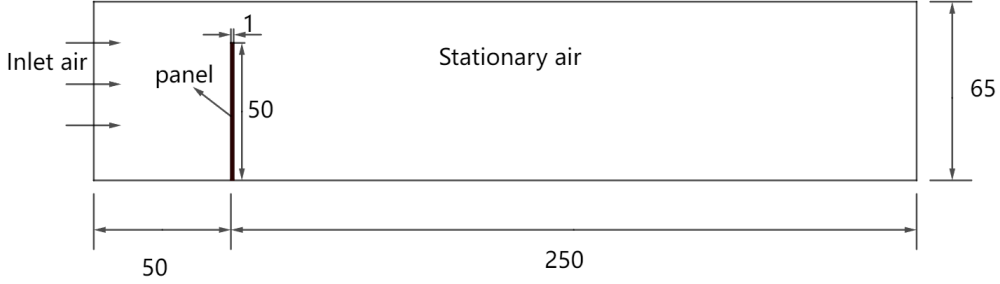


Figure 12: Simplified geometric configuration for numerical simulation.

Table 3: Fluid properties and flow conditions for the simulation.

Material	Density (kg/m^3)	Pressure (Pa)	Specific Heat Ratio	Velocity (m/s)
Stationary air	1.20	101.0	1.4	0
Inflow air	1.63	155.7	1.4	109.6

comparable to the domain size in the y -direction, a uniform grid is adopted in the y -direction, with a grid spacing of $\Delta y = 0.02L$.

Figure 13 shows the comparison of the Schlieren images between [65] and our simulation results. Figure 14 shows the displacement of the panel’s end during the loading process over 2 ms, based on both the experimental and current simulation data. The numerical results show good agreement with the experimental data [65]. In the time range from 0 to about 1.5 ms, the displacement increase is consistent with the experimental data. After 1.5 ms, the decrease in displacement also agrees well with the experimental results.

4.4. Fracture inside a cylinder induced by supersonic flow

Finally, we consider a typical supersonic fluid-solid interaction scenario. In this case, the free stream moving of Mach number 1.7 impacts a cylinder that contains a pre-existing internal crack. Upon impact, the crack propagates, showcasing the distinct advantages of the current PD-based FSI model.

The supersonic flow with $\text{Ma} = 1.7$ and $\text{Re} = 200,000$ is considered in the simulation. The computational domain spans $(0,10D) \times (0,12D)$, with the cylinder center located at $(2D,6D)$. A non-uniform grid is used with a fine grid ($\Delta x = \Delta y = D/128$) near the cylinder and a coarser grid ($\Delta x = \Delta y = D/2$) in the distant regions. The material is assumed to be isotropic and linear elastic with the density of 100 kg/m^3 . The distance between material points is $\Delta x = 0.005$, and the horizon size is set as $\delta = 4\Delta x$. An initial crack is pre-defined inside the cylinder, as shown in Figure 15.

Figure 16 shows the Mach number distribution around the upper half of the cylinder, and Figure 17 illustrates crack propagation inside the cylinder under flow impact for different values of Young’s modulus. For Young’s moduli of 30 MPa, 40 MPa, and 50 MPa, the crack bifurcates as it propagates to the right, with a bifurcation angle of approximately 130° . The

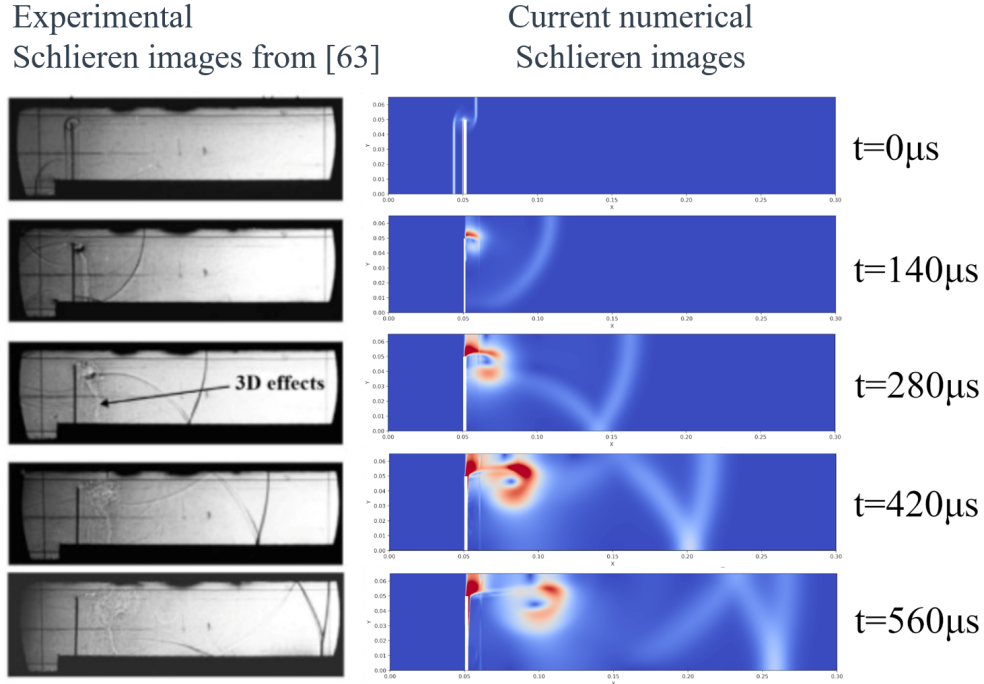


Figure 13: Comparison between the time evolution of (a) the experimental Schlieren photos from [65] and (b) our numerical results for the panel with 50 mm length.

curvature of the bifurcated crack increases with the Young's modulus. However, when the Young's modulus reaches 60 MPa, the behavior reverses, and the crack bifurcates to the left, with a bifurcation angle of around 70° . The results of numerical experiments show that different flow properties and physical parameters are decisive for the mode and rate of crack extension. This fully justifies the need to develop coupled flow-solid solvers that can be applied to fracture mechanics.

5. Conclusion

In this work, we present a novel hybrid algorithm that seamlessly couples compressible fluid mechanics with deformable material behavior within a unified mesoscopic framework. The gas-kinetic scheme and bond-based peridynamics are utilized to characterize the dynamics of fluids and solids, respectively. The integration of these two methods via the ghost-cell immersed boundary method facilitates a synchronized evolution of both fluid and solid fields.

The extensive numerical experiments, including subsonic and supersonic flows around canonical geometries, crack propagation, and shock wave impacts on elastic panels, demonstrate the algorithm's efficacy and its ability to predict the deformation, damage, and fracture of materials caused by high-speed flows. These results underscore the method's potential to address challenging fluid-structure interaction problems that are difficult to solve with the traditional approaches.

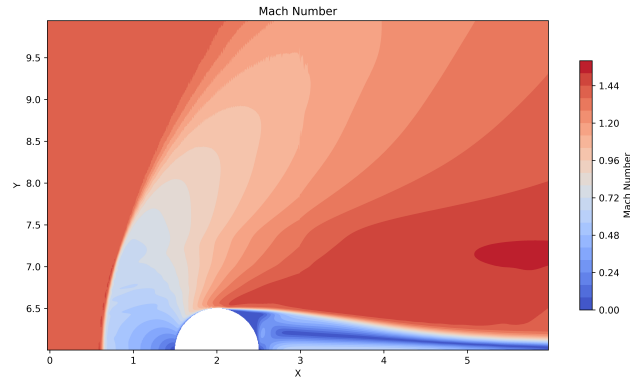


Figure 16: Mach number distribution in the flow field around the cylinder.

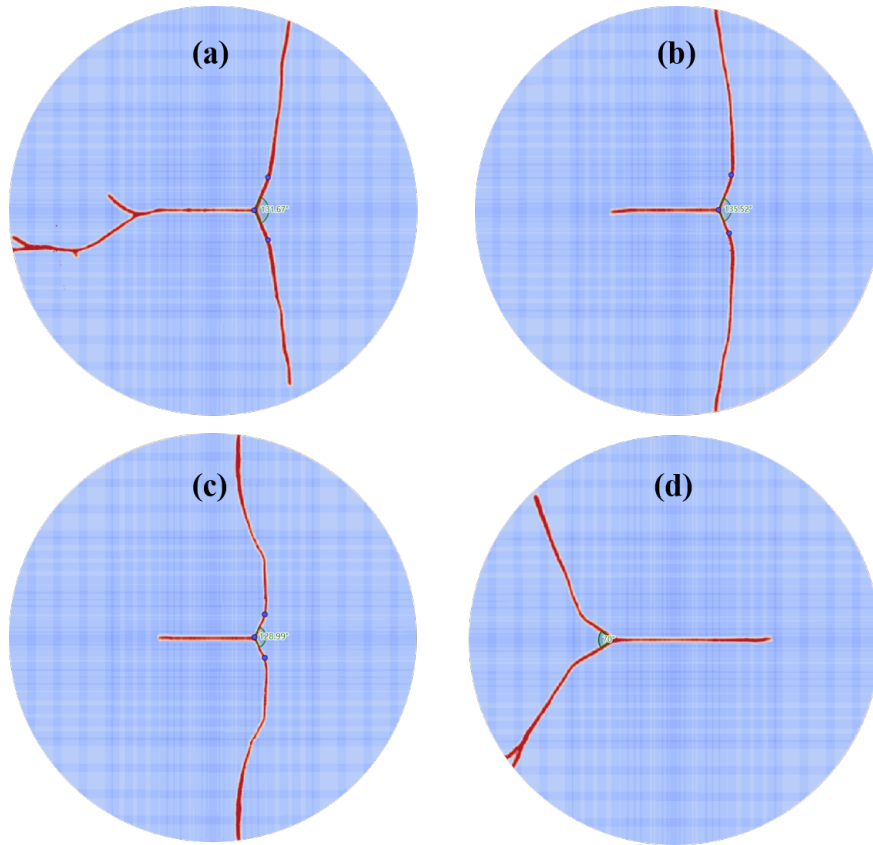


Figure 17: Fracture in the cylinder induced by a supersonic flow. The cylinders in (a), (b), (c), and (d) have the Young's moduli of 30 MPa, 40 MPa, 50 MPa, and 60 MPa, respectively.

Acknowledgment

The current research is funded by the National Science Foundation of China (No. 12302381) and the Chinese Academy of Sciences Project for Young Scientists in Basic Research (YSBR-107). The computing resources provided by Hefei Advanced Computing Center and ORISE

Supercomputer are acknowledged.

References

- [1] D. Szirczak, H. Smith, A review of design issues specific to hypersonic flight vehicles, *Progress in Aerospace Sciences* 84 (2016) 1–28.
- [2] E. H. Dowell, K. C. Hall, Modeling of fluid-structure interaction, *Annual Review of Fluid Mechanics* 33 (Volume 33, 2001) (2001) 445–490.
- [3] R. Kamakoti, W. Shyy, Fluid–structure interaction for aeroelastic applications, *Progress in Aerospace Sciences* 40 (8) (2004) 535–558.
- [4] M. Souli, D. J. Benson, *Arbitrary Lagrangian Eulerian and fluid-structure interaction: numerical simulation*, John Wiley & Sons, 2013.
- [5] T. E. Tezduyar, S. Sathe, J. Pausewang, M. Schwaab, J. Christopher, J. Crabtree, Interface projection techniques for fluid–structure interaction modeling with moving-mesh methods, *Computational Mechanics* 43 (2008) 39–49.
- [6] R. Verzicco, Immersed boundary methods: Historical perspective and future outlook, *Annual Review of Fluid Mechanics* 55 (1) (2023) 129–155.
- [7] F. Sotiropoulos, X. Yang, Immersed boundary methods for simulating fluid–structure interaction, *Progress in Aerospace Sciences* 65 (2014) 1–21.
- [8] R. Mittal, J. H. Seo, Origin and evolution of immersed boundary methods in computational fluid dynamics, *Physical Review Fluids* 8 (2023) 100501.
- [9] B. Kallemov, A. Bhalla, B. Griffith, A. Donev, An immersed boundary method for rigid bodies, *Communications in Applied Mathematics and Computational Science* 11 (1) (2016) 79–141.
- [10] C.-C. Liao, Y.-W. Chang, C.-A. Lin, J. McDonough, Simulating flows with moving rigid boundary using immersed-boundary method, *Computers & Fluids* 39 (1) (2010) 152–167.
- [11] Y. Kim, C. S. Peskin, A penalty immersed boundary method for a rigid body in fluid, *Physics of Fluids* 28 (3) (2016).
- [12] S.-W. Su, M.-C. Lai, C.-A. Lin, An immersed boundary technique for simulating complex flows with rigid boundary, *Computers & fluids* 36 (2) (2007) 313–324.
- [13] W.-X. Huang, C. B. Chang, H. J. Sung, An improved penalty immersed boundary method for fluid–flexible body interaction, *Journal of Computational Physics* 230 (12) (2011) 5061–5079.
- [14] A. Gilmanov, F. Sotiropoulos, A hybrid cartesian/immersed boundary method for simulating flows with 3d, geometrically complex, moving bodies, *Journal of computational physics* 207 (2) (2005) 457–492.
- [15] J. Favier, A. Revell, A. Pinelli, A lattice boltzmann–immersed boundary method to simulate the fluid interaction with moving and slender flexible objects, *Journal of Computational Physics* 261 (2014) 145–161.
- [16] I. Lee, H. Choi, A discrete-forcing immersed boundary method for the fluid–structure interaction of an elastic slender body, *Journal of Computational Physics* 280 (2015) 529–546.
- [17] J.-I. Choi, R. C. Oberoi, J. R. Edwards, J. A. Rosati, An immersed boundary method for complex incompressible flows, *Journal of Computational Physics* 224 (2) (2007) 757–784.
- [18] X. Yang, X. Zhang, Z. Li, G.-W. He, A smoothing technique for discrete delta functions with application to immersed boundary method in moving boundary simulations, *Journal of Computational Physics* 228 (20) (2009) 7821–7836.
- [19] D. Xu, J. Liu, Y. Wu, C. Ji, A high-efficiency discretized immersed boundary method for moving boundaries in incompressible flows, *Scientific Reports* 13 (1) (2023) 1699.
- [20] M. H. A. Azis, F. Evrard, B. van Wachem, An immersed boundary method for incompressible flows in complex domains, *Journal of Computational Physics* 378 (2019) 770–795.
- [21] S. Dutta, C. S. Jog, A monolithic arbitrary lagrangian–eulerian-based finite element strategy for fluid–structure interaction problems involving a compressible fluid, *International Journal for Numerical Methods in Engineering* 122 (21) (2021) 6037–6102.

- [22] F.-B. Tian, H. Dai, H. Luo, J. F. Doyle, B. Rousseau, Fluid–structure interaction involving large deformations: 3d simulations and applications to biological systems, *Journal of Computational Physics* 258 (2014) 451–469.
- [23] F. D. Vanna, F. Picano, E. Benini, A sharp-interface immersed boundary method for moving objects in compressible viscous flows, *Computers & Fluids* 201 (2020) 104415.
- [24] R. Ghias, R. Mittal, H. Dong, A sharp interface immersed boundary method for compressible viscous flows, *Journal of Computational Physics* 225 (1) (2007) 528–553.
- [25] J. Ning, H. Zhang, X. Xu, T. Ma, A novel fluid-structure interaction algorithm for compressible flows and deformable structures, *Journal of Computational Physics* 426 (2021) 109921.
- [26] L. Wang, J. Young, F.-B. Tian, An immersed boundary method for the thermo–fluid–structure interaction in rarefied gas flows, *Physics of Fluids* 36 (1) (2024) 013616.
- [27] A. Shahani, M. A. Fasakhodi, Finite element analysis of dynamic crack propagation using remeshing technique, *Materials & design* 30 (4) (2009) 1032–1041.
- [28] L. Ramalho, J. Belinha, R. Campilho, A novel robust remeshing finite element technique for fracture propagation, *International Journal of Computational Methods* 18 (02) (2021) 2050040.
- [29] N. Moes, J. Dolbow, T. Belytschko, A finite element method for crack growth without remeshing, *International Journal for Numerical Methods in Engineering* 46 (1) (1999) 131–150.
- [30] T. Fries, Overview and comparison of different variants of the xfem, *Pamm* 14 (1) (2014) 27–30.
- [31] S. A. Silling, Reformulation of elasticity theory for discontinuities and long-range forces, *Journal of the Mechanics and Physics of Solids* 48 (1) (2000) 175–209.
- [32] S. A. Silling, M. Epton, O. Weckner, J. Xu, E. Askari, Peridynamic states and constitutive modeling, *Journal of Elasticity* 88 (2) (2007) 151–184.
- [33] Y. Zhang, G. Pan, Y. Zhang, S. Haeri, A multi-physics peridynamics-dem-ib-clbm framework for the prediction of erosive impact of solid particles in viscous fluids, *Computer Methods in Applied Mechanics and Engineering* 352 (2019) 675–690.
- [34] S. Oterkus, E. Madenci, A. Agwai, Fully coupled peridynamic thermomechanics, *Journal of the Mechanics and Physics of Solids* 64 (1) (2014) 1–23.
- [35] E. Madenci, E. Oterkus, *Peridynamic theory and its applications*, Vol. 9781461484653 of *Peridynamic Theory and Its Applications*, Springer New York, NY, 2014.
- [36] H. Zhang, D. Huang, X. Zhang, Peridynamic modeling of elastic-plastic ductile fracture, *Computer Methods in Applied Mechanics and Engineering* 418 (2024) 116560.
- [37] D. Yang, X. He, Y. Deng, An effective correspondence-based peridynamics-fem coupling model for brittle fracture, *International Journal of Mechanical Sciences* 264 (2024) 108815.
- [38] H. Wang, L. Wu, J. Guo, C. Yu, Y. Li, Y. Wu, Three-dimensional modeling and analysis of anisotropic materials with quasi-static deformation and dynamic fracture in non-ordinary state-based peridynamics, *Applied Mathematical Modelling* 125 (2024) 625–648.
- [39] L. Zhou, S. Zhu, Z. Zhu, Cosserat ordinary state-based peridynamic model and numerical simulation of rock fracture, *Computers and Geotechnics* 155 (2023) 105240.
- [40] Z. Yang, S. Zheng, F. Han, J. Cui, An efficient peridynamics-based statistical multiscale method for fracture in composite structures, *International Journal of Mechanical Sciences* 259 (2023) 108611.
- [41] S. Jafarzadeh, F. Mousavi, A. Larios, F. Bobaru, A general and fast convolution-based method for peridynamics: Applications to elasticity and brittle fracture, *Computer Methods in Applied Mechanics and Engineering* 392 (2022) 114666.
- [42] D. A. Abdoh, B. B. Yin, V. K. R. Kodur, K. M. Liew, Computationally efficient and effective peridynamic model for cracks and fractures in homogeneous and heterogeneous materials, *Computer Methods in Applied Mechanics and Engineering* 399 (2022) 115318.
- [43] J. M. Zhan, X. H. Yao, F. Han, An approach of peridynamic modeling associated with molecular dynamics for fracture simulation of particle reinforced metal matrix composites, *Composite Structures* 250 (2020) 112613.
- [44] S. Hu, T. Xiao, M. Han, Z. Li, E. Oterkus, S. Oterkus, Y. Zhang, An efficient explicit-implicit adaptive method for peridynamic modelling of quasi-static fracture formation and evolution, *arXiv preprint*

- arXiv:2410.12552 (2024).
- [45] Y. Gao, S. Oterkus, Fluid-elastic structure interaction simulation by using ordinary state-based peridynamics and peridynamic differential operator, *Engineering Analysis with Boundary Elements* 121 (2020) 126–142.
 - [46] M. Behzadinasab, G. Moutsanidis, N. Trask, J. T. Foster, Y. Bazilevs, Coupling of iga and peridynamics for air-blast fluid-structure interaction using an immersed approach, *Forces in Mechanics* 4 (2021) 100045.
 - [47] S. Shende, M. Behzadinasab, G. Moutsanidis, Y. Bazilevs, Simulating air blast on concrete structures using the volumetric penalty coupling of isogeometric analysis and peridynamics, *Mathematical Models and Methods in Applied Sciences* 32 (12) (2022) 2477–2496.
 - [48] Y. Zhang, S. Haeri, G. Pan, Y. Zhang, Strongly coupled peridynamic and lattice boltzmann models using immersed boundary method for flow-induced structural deformation and fracture, *Journal of Computational Physics* 435 (2021) 110267.
 - [49] F. Dalla Barba, M. Zaccariotto, U. Galvanetto, F. Picano, 3d fluid–structure interaction with fracturing: A new method with applications, *Computer Methods in Applied Mechanics and Engineering* 398 (2022) 115210.
 - [50] K. H. Kim, A. P. S. Bhalla, B. E. Griffith, An immersed peridynamics model of fluid-structure interaction accounting for material damage and failure, *Journal of Computational Physics* 493 (2023) 112466.
 - [51] K. Xu, A gas-kinetic bgk scheme for the navier–stokes equations and its connection with artificial dissipation and godunov method, *Journal of Computational Physics* 171 (1) (2001) 289–335.
 - [52] S. Chen, K. Xu, Z. Li, Cartesian grid method for gas kinetic scheme on irregular geometries, *Journal of Computational Physics* 326 (2016) 862–877.
 - [53] T. Xiao, C. Liu, K. Xu, Q. Cai, A velocity-space adaptive unified gas kinetic scheme for continuum and rarefied flows, *Journal of Computational Physics* 415 (2020) 109535.
 - [54] P. L. Bhatnagar, E. P. Gross, M. Krook, A model for collision processes in gases. i. small amplitude processes in charged and neutral one-component systems, *Physical review* 94 (3) (1954) 511.
 - [55] E. Shakhov, Generalization of the krook kinetic relaxation equation, *Fluid Dynamics* 3 (5) (1968) 95–96.
 - [56] L. H. Holway Jr, New statistical models for kinetic theory: methods of construction, *Physics of Fluids* (1958-1988) 9 (9) (1966) 1658–1673.
 - [57] K. Xu, *Direct modeling for computational fluid dynamics: construction and application of unified gas-kinetic schemes*, Vol. 4, World Scientific, 2014.
 - [58] T. Xiao, A flux reconstruction kinetic scheme for the boltzmann equation, *Journal of Computational Physics* 447 (2021) 110689.
 - [59] T. Xiao, *Kinetic. jl: A portable finite volume toolbox for scientific and neural computing*, *Journal of Open Source Software* 6 (62) (2021) 3060.
 - [60] S. Oterkus, E. Madenci, Peridynamic modeling of fuel pellet cracking, *Engineering Fracture Mechanics* 176 (2017) 23–37.
 - [61] Y. Sun, Z. Wang, Y. Liu, Spectral (finite) volume method for conservation laws on unstructured grids vi: Extension to viscous flow, *Journal of Computational Physics* 215 (1) (2006) 41–58.
 - [62] K. Luo, C. Mao, Z. Zhuang, J. Fan, N. E. L. Haugen, A ghost-cell immersed boundary method for the simulations of heat transfer in compressible flows under different boundary conditions part-ii: Complex geometries, *International Journal of Heat and Mass Transfer* 104 (2017) 98–111.
 - [63] S. Takahashi, T. Nonomura, K. Fukuda, A numerical scheme based on an immersed boundary method for compressible turbulent flows with shocks: Application to two-dimensional flows around cylinders, *Journal of Applied Mathematics* 2014 (1) (2014) 252478.
 - [64] E. Madenci, E. Oterkus, *Nonimpact problems*, in: *Peridynamic Theory and Its Applications*, Springer New York, New York, NY, 2014, pp. 171–180.
 - [65] J. Giordano, G. Jourdan, Y. Burtschell, M. Medale, D. E. Zeitoun, L. Houas, Shock wave impacts on deforming panel, an application of fluid-structure interaction, *Shock Waves* 14 (1) (2005) 103–110.